A&A, 692, A3 (2024)
https://doi.org/10.1051/0004-6361/202449783

Astronomy & Astrophysics

Early photometric and spectroscopic observations of the extraordinarily bright INTEGRAL-detected GRB 221009A

R. Sánchez-Ramírez[1,⋆], R. G. Lang[2], A. Pozanenko[3,4,5], H. Martínez-Huerta[6], Y.-D. Hu[1,35], S. B. Pandey[7], R. Gupta[7,8,9], A. K. Ror[7,32,⋆], B.-B. Zhang[10,11], M. D. Caballero-García[1], S. R. Oates[12], I. Pérez-García[1], S. Guziy[1,13], E. J. Fernández-García[1], S.-Y. Wu[1], L. Almeida[14], A. Aryan[7], S. Belkin[3,4,34], C. R. Bom[15,16], M. Butner[17], O. Burkhonov[18], I. Carrasco-García[19], A. Castellón[19], M. A. Castro Tirado[1,19], I. Chelovekov[3], Sh. A. Egamberdiyev[7], R. García-Benito[1], S. A. García González[1], S. Grebenev[3], C. D. Kilpatrick[20], E. Klunko[21], M. Makler[15,22], P. Minaev[3], A. Mkrtchyan[5], A. Moskvitin[23], F. Navarete[24], A. Novichonok[33], N. Pankov[5,6], M. Passas-Varo[1], C. Pérez del Pulgar[19], A. Reina Terol[19], J. A. Smith[25], S. Tinyanont[26], D. L. Tucker[27], R. Uklein[23], A. Volnova[3], M. P. Wiesner[28], M. Gritsevich[29,30,31], and A. J. Castro-Tirado[1,19]

(Affiliations can be found after the references)

Received 28 February 2024 / Accepted 5 September 2024

ABSTRACT

Context. GRB 221009A, initially detected as an X-ray transient by *Swift*, was later revealed to have triggered the *Fermi* satellite about an hour earlier, marking it as a post-peak observation of the event's emission. This GRB distinguished itself as the brightest ever recorded, presenting an unparalleled opportunity to probe the complexities of GRB physics. The unprecedented brightness, however, challenged observation efforts, as it led to the saturation of several high-energy instruments.

Aims. Our study seeks to investigate the nature of the INTEGRAL-detected GRB 221009A and elucidate the environmental conditions conducive to these exceptionally powerful bursts. Moreover, we aim to understand the fundamental physics illuminated by the detection of teraelectronvolt (TeV) photons emitted by GRB 221009A.

Methods. We conducted detailed analyses of early photometric and spectroscopic observations that span from the *Fermi* trigger through to the initial days following the prompt emission phase in order to characterize GRB 221009A's afterglow, and we complemented these analyses with a comparative study.

Results. Our findings from analyzing INTEGRAL data confirm GRB 221009A as the most energetic event observed to date. Early optical observations during the prompt phase negate the presence of bright optical emissions with internal or external shock origins. Spectroscopic analyses enabled us to measure GRB 221009A's distance and line-of-sight properties. The afterglow's temporal and spectral analysis suggests prolonged activity of the central engine and a transition in the circumburst medium's density. Finally, we discuss the implications for fundamental physics of detecting photons as energetic as 18 TeV from GRB 221009A.

Conclusions. Early optical observations have proven invaluable for distinguishing between the potential origins of optical emissions in GRB 221009A, underscoring their utility in GRB physics studies. However, the rarity of such data underscores the need for dedicated telescopes capable of synchronous multiwavelength observations. Additionally, our analysis suggests that the host galaxies of TeV GRBs share commonalities with those of long and short GRBs. Expanding the sample of TeV GRBs could further solidify these findings.

Key words. techniques: photometric – techniques: spectroscopic – gamma-ray burst: general – gamma-ray burst: individual: GRB 221009A

1. Introduction

The study of gamma-ray burst (GRB) prompt emission and its afterglow has been crucial in advancing high-energy astrophysical research at the cosmic scale. However, GRBs, which are traditionally classified as long GRBs (lGRB; from stellar collapses, $T_{90} \gtrsim 2$ s) or short GRBs (sGRBs; from compact object mergers, $T_{90} \lesssim 2$ s), have faced severe challenges recently (Kouveliotou et al. 1993; Ahumada et al. 2021; Troja et al. 2022; Rastinejad et al. 2022; Levan et al. 2024). The collision of a relativistic blast wave with the circumburst medium generates external shocks, leading to a multiwavelength afterglow phase. This afterglow is essential for understanding the progenitor and the surrounding environment (Mészáros & Rees 1997; Sari et al. 1998; Piran 2004; Caballero-García et al. 2023). The *Swift* satellite's rapid localization, along with a prompt response from robotic optical telescopes, allows for early afterglow observations, providing insights into these events (Gehrels et al. 2004; Akerlof et al. 1999; Pandey & Zheng 2013; Gupta et al. 2021a; Castro-Tirado 2023).

On October 9, 2022, at 14:10 UT, a new bright and hard X-ray transient, Swift J1913.1+1946, was detected by *Swift*, marking an unprecedented discovery in the field of high-energy astrophysics (Dichiara et al. 2022). Located at RA(J2000) = 288.26452 and Dec(J2000) = 19.7735, this transient was initially thought to be of Galactic origin due to its proximity, 4.32°, to the Galactic plane. Subsequent observations, however, unveiled a more complex nature. Approximately one hour prior to the *Swift* detection, at 13:16:59 UT, *Fermi*/GBM had already captured signals from the event, and shortly after, at 14:17:06 UT, *Fermi*/LAT reported the detection of GeV photons. Moreover, *Konus*-Wind detected a long tail post prompt emission extending up to 20 ks (Frederiks et al. 2023). This sequence of events not only broadened our understanding of this source but also led to the transient being identified as GRB 221009A,

⋆ Corresponding authors; ruben.sanchez@csic.es, amitror@aries.res.in

and it was subsequently recognized as one of the brightest GRBs ever (The BOAT; Burns et al. 2023) observed (Veres et al. 2022), with an occurrence rate of ≤1 per 1000 yr (Williams et al. 2023).

In this paper, we present a detailed analysis of the high-energy observations of GRB 221009A made available through INTEGRAL alongside a comprehensive examination of early photometric and spectroscopic data collected via our optical/nIR observing programs. Our analysis delves into the temporal and spectral characteristics of GRB 221009A, offering new insights into the nature of this remarkable event. Additionally, we explore the characteristics of the host galaxy, including its mass, star formation rate (SFR), and specific star formation rate (sSFR), comparing these attributes to those of other TeV-detected GRBs and the host galaxies of both long and short bursts. Finally, we discuss the implications of detecting extremely high energy photons, up to 18 TeV, from GRB 221009A. This observation not only challenges existing theoretical models but also offers potential insights into fundamental physics.

The structure of this paper is as follows: Section 2 outlines our observational and data reduction methodologies for GRB 221009A, spanning both INTEGRAL and optical/nIR data. Section 3 presents the key findings from our investigation. The paper culminates in Section 4 with a discussion of the implications of our results, and this is followed by a concise summary and conclusion in Section 5. Errors throughout the paper are reported at the 1σ confidence level, unless otherwise stated.

2. Observations

2.1. High-energy INTEGRAL observations

The prompt emission of GRB 221009A (Kennea & Williams 2022) was detected by the Anti-Coincidence Shield (ACS) of the gamma-ray spectrometer, SPectrometer on INTEGRAL (SPI), on board the International Gamma-Ray Astrophysics Laboratory (INTEGRAL) observatory (Gotz et al. 2022) as well as by the Anti-Coincidence Shield (VETO) of the INTEGRAL Soft Gamma-Ray Imager (ISGRI) mounted on the softer gamma-ray telescope, Imager on Board the INTEGRAL Satellite (IBIS). In this work, we examine the prompt temporal data of GRB 221009A registered by this observatory.

2.2. Early photometric observations

2.2.1. Optical photometry from Mondy, Maidanak, and Kitab observatories

The all-sky camera at the Mondy Observatory, operated by the Institute of Solar-Terrestrial Physics of the Siberian Branch of the Russian Academy of Sciences and located near the village of Mondy in Buryatia, Russia, monitored the region encompassing the GRB 221009A. This instrument acquired an optical image with an integration time starting before T_0, that is, preceding the Gamma-ray Burst Monitor (GBM) trigger. Despite the extensive coverage, no optical counterpart to GRB 221009A was detected within this time frame. Consequently, we established an upper limit of 6 mag for any potential optical counterpart during these initial epochs.

Follow-up observations of the GRB's location commenced on October 9, 2022, at 14:26:54 UT, utilizing the CCD photometer attached to the 1.6 m AZT-33IK telescope at the Mondy Observatory. These observations were performed with an R-filter, as described by Belkin et al. (2022a). A sequence of exposures, each lasting between 90 and 120 s, was captured until 15:34:05 UT. The GRB's afterglow is clearly detected in each individual frame. Additional observations were conducted using the 1.5 m AZT-22 telescope at the Mount Maidanak Observatory, operated by the Ulugh Beg Astronomical Institute (UBAI) of the Uzbek Academy of Sciences, situated in southern Uzbekistan, and the 0.36 m ISON RC-36 telescope at the Kitab Observatory (KO UzAS).

Image processing of this data set was performed using standard routines within the Image Reduction and Analysis Facility (IRAF)[1], following established methodologies (Tody 1986, 1993). Photometric calibration was achieved by comparing with nearby stars cataloged in the USNO-B1.0 database, specifically the R2 magnitude set. The calibrated magnitudes obtained from these observations are detailed in Table A.1.

2.2.2. BOOTES network observations

The 0.6 m robotic TeLescope of MAlaga (TELMA) at the Burst Observer and Optical Transient Exploring System station 2 (BOOTES-2) is located at the IHSM La Mayora (UMA-CSIC) in Algarrobo Costa (Málaga, Spain). TELMA responded to the GRB 221009A soon after twilight, specifically, 18:23:06 UT on October 9, 2022 (Hu et al. 2022). A number of 60-s images were taken under poor weather conditions.

Later on, we triggered the 0.6 m BOOTES-5/JGT (Javier Gorosabel Telescope) at the Observatorio Astronómico Nacional in San Pedro Martir (Mexico). A couple of 60-s exposures were obtained in the r-band starting on October 11, 2022, at 06:14:33 UT.

We reduced and performed aperture photometry using IRAF, calibrating against several reference stars from the Pan-STARRS catalog. The optical counterpart is barely detected in these images (see Table A.1).

2.2.3. 0.9 m OSN telescope follow-up

The 0.9 m telescope of the Sierra Nevada Observatory (OSN; Granada, Spain) started to observe the location of the GRB at 18:45:18.20 UT on October 9, 2022 (T_0 + ~5.5 h). A series of images were obtained in the Johnson-Cousins broad-band filters BVRI across several nights.

Photometric results were derived using the same prescription as the BOOTES data, using the transformation equation found by Lupton in 2005[2]. The brightness values in different filters are tabulated in Table A.1.

2.2.4. CAHA 2.2 m telescope

We also triggered, with our ToO program, the 2.2 m Calar Alto Hispano-Alemían (CAHA) telescope at the Calar Alto Observatory in Almería, Spain. Using the mounted instrument Calar Alto Faint Object Spectrograph (CAFOS). Two epochs of observations were executed on October 14 and 17, 2022 (i.e., T_0+5.3 d and T_0 + 8.3 d, respectively), using Sloan-griz filters. The afterglow is clearly detected in the stacked image of both epochs. After bias and flat field corrections, standard procedures using IRAF routines were performed to obtain the aperture photometry. Results were calibrated using Pan-STARRS stars in the same field. The full observation log is provided in Table A.1.

[1] https://iraf-community.github.io
[2] https://classic.sdss.org/dr4/algorithms/sdssUBVRITransform.html

Table 1. Log of the spectroscopic observations of GRB 221009A.

T–T$_0$ (days)	Wavelength range (Å)	Grism	Exposure (s)	Instrument
0.391	3630–7500	R1000B	2×900	GTC/OSIRIS
0.409	5100–10 000	R1000R	2×300	GTC/OSIRIS
3.425	9500–24700	3500	12×220	SOAR/TripleSpec
9.157	3500–8500	VPHG940	7×1200	BTA/SCORPIO-2

2.2.5. Observations with the IRTF 3.2 m telescope

On October 25, 2022, we activated the 3.2-meter InfraRed Telescope Facility (IRTF) situated at the Mauna Kea Observatory in Hawaii, USA, to monitor the burst region. We acquired near-infrared observations in both the J and K bands, employing continuous exposures of 50 s each. The target was successfully detected in the stacked image. We performed aperture photometry calibrated against the Two Micron All Sky Survey (2MASS) catalog standards. The photometric data are presented in Table A.1, facilitating comparison and further analysis (see Table 1).

2.3. Spectroscopy

2.3.1. 10.4 m GTC (+OSIRIS) early optical spectroscopy

We observed the optical afterglow of GRB 221009A using the Optical System for Imaging and low-Resolution Integrated Spectroscopy (OSIRIS; Cepa et al. 2000) mounted on the 10.4 m Gran Telescopio de Canarias (GTC) at the Roque de los Muchachos Observatory (La Palma, Spain). The observations were carried out under favorable conditions (clear and dark night, seeing ∼0.7″). They consisted of 2×900 s spectra with grism R1000B and 2×300 s with grism R1000R, using a 1″ slit, overall covering the wavelength range between 3770 Å and 10 000 Å. The science data acquisition started at 22:32:00 UT on October 9, 2022, which corresponds to an average epoch of 0.362 days after the burst (Castro-Tirado et al. 2022).

The data set was reduced using standard procedures under IRAF v1.17. In brief, individual frames were processed for bias and flat-fielding. After that, wavelength calibrations were calculated using Hg, Ar, Ne, and Xe arc frames. Lastly, the science spectra were stacked, extracted, and flux calibrated using the spectrophotometric standard Feige 110. We also accounted for slit losses by scaling the spectra to the photometry of the acquisition images ($r' = 17.14 \pm 0.05$ and $i' = 16.12 \pm 0.01$), correcting for an attenuation of ∼25%. The stacked spectrum is shown in the left panel of Figure 1.

2.3.2. SOAR TripleSpec near infra-red spectroscopy

On October 12, 2022, the optical afterglow of GRB 221009A was clearly visible in the NIR (Figure 2). We observed the afterglow with the TripleSpec4.1 (Schlawin et al. 2014) near-infrared (NIR) spectrograph at the 4.1 m SOuthern Astrophysical Research (SOAR) telescope located at Cerro Pachón, Chile. TripleSPec4.1 is a cross-dispersed single-object long-slit infrared imaging spectrograph that covers a simultaneous wavelength range of 0.95 to 2.47 microns at a spectral resolution of approximately 3500 in five spectral orders, encompassing the entire z'YJHK photometric range. We took 12 short (220 s) exposures in order to not saturate the telluric lines using the ABBA dither pattern, observing a standard star after each ABBA sequence. We reduced all TripleSpec data following standard procedures in `spextool` (Cushing et al. 2004) and performed telluric corrections with `xtellcor` (Vacca et al. 2003). The reduced spectrum is shown in the Figure 2. High brightness and rather shallow afterglow evolution at NIR frequencies (discussed in successive sections) of this nearby GRB allowed us to obtain a typical featureless spectrum more than 3.4 d post burst.

2.3.3. 6 m BTA (+SCORPIO-2) late optical spectroscopy

We observed the counterpart of GRB 221009A on October 18, 2022, with the Spectral Camera with Optical Reducer for Photometric and Interferometric Observations (SCORPIO-2; Afanasiev & Moiseev 2011) mounted on the 6 m BTA telescope at the Special Astrophysical Observatory of the Russian Academy of Science (SAO RAS) in North Caucasus, Russia. The observations were carried out under good conditions (seeing ∼1.5″). A total of 7×1200 s spectra were obtained using grism VPHG940@600 combined with a 1.0″ slit, overall covering the spectral range between 3500 Å and 8500 Å (right panel of Figure 1). The data were reduced in the same manner as the OSIRIS data. In this case, flux calibration was performed against the spectrophotometric standard BD+75d325.

3. Results

3.1. Prompt emission

We present the high-energy light curve of GRB 221009A as observed by the INTEGRAL satellite in Figure 3. This light curve, derived from the ACS of the SPI instrument, exhibits a complex temporal structure characterized by two primary episodes and an initial, less intense precursor emission. The precursor emission was initiated at 13:16:58 UT, persisting for approximately 17 s. The principal burst phase commenced at T_0 = 13:19:52 UT, showcasing a multipeaked profile over a span of roughly 310 s, as described by Gotz et al. (2022) and depicted in Figure 3.

The GRB position angular distance is 60 degrees off axis relative to the X-axes (center of the field of view of both SPI and IBIS/ISGRI telescopes), and it positioned the target outside the nominal field of view for both telescopes. Despite this, the light curves captured through the protective shields during the main burst phase were subject to saturation. This saturation affected the ACS and a significant portion of the VETO-ISGRI detectors. To circumvent this issue and estimate the unsaturated count rate, we calibrated against data from the Mini-Calorimeter (MCAL) detector within the VETO-ISGRI array, which remained unaffected by saturation.

Additionally, we incorporated observations from the Mercury Gamma-ray and Neutron Spectrometer (MGNS) aboard the *BepiColombo* spacecraft, covering the energy range of 280–460 keV (Kozyrev et al. 2022). By using the light curves from both the MCAL and MGNS detectors, we fitted the lower-intensity segment of the SPI-ACS light curve (from 380 s to 498 s post T_0), which was presumably free from detector dead time effects. Through this analysis, we derived a scaling coefficient ($k = 7.99 \pm 0.07$) between the INTEGRAL SPI-ACS detector and the INTEGRAL IBIS-VETO detector, enabling us to model the unsaturated SPI-ACS light curves accurately. Figure 3 illustrates both the original saturated SPI-ACS light curve and the adjusted models that represent the unsaturated emission profile.

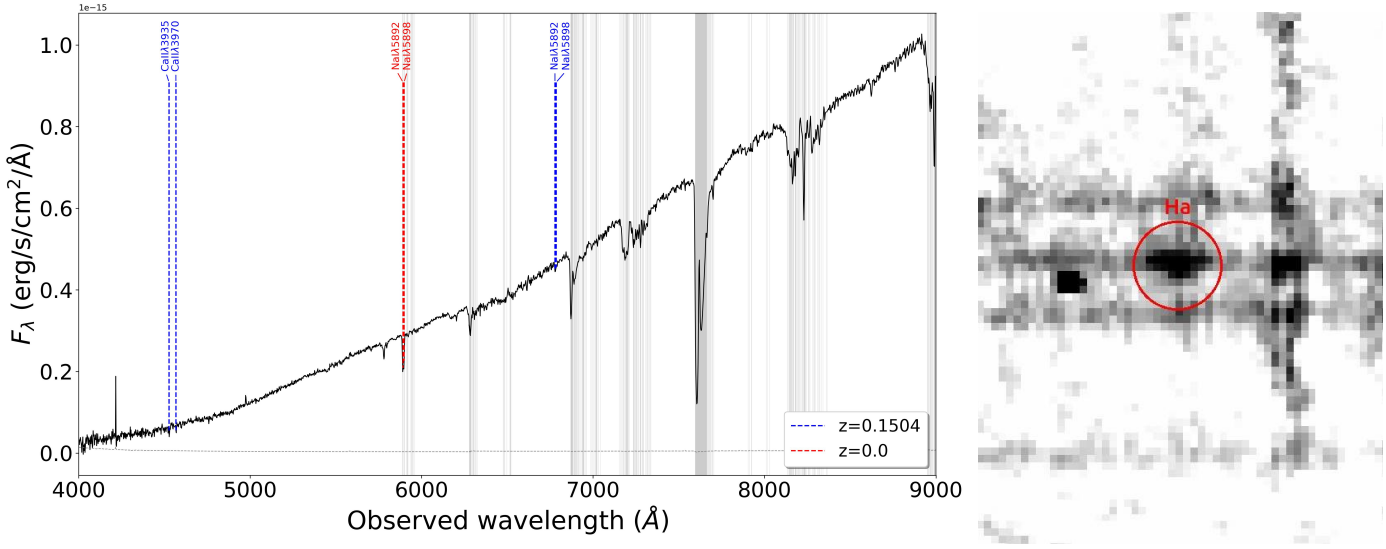

Fig. 1. Line identification of GRB 221009A. Left. GRB 221009A afterglow optical spectrum as observed by the 10.4 m GTC(+OSIRIS) 8.6 hours post burst. The signal is represented by the solid black line, and the error spectrum is indicated with the gray dotted line. Vertical gray lines and bands represent the regions affected by telluric absorption. Identified lines at a given redshift are marked following the color code shown in the plot. Right. Hα line observed by the 6m BTA(+SCORPIO-2) on October 18, 2022. With the analysis of these early spectra, we established a redshift of GRB 221009A to be 0.151.

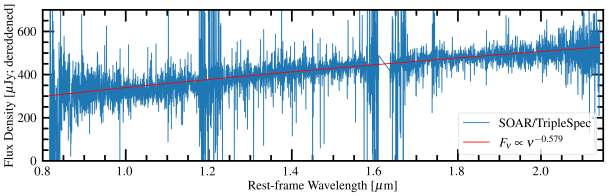

Fig. 2. Spectrum of GRB 221009A obtained with the TripleSpec spectrograph on the SOAR 4.1 m telescope.

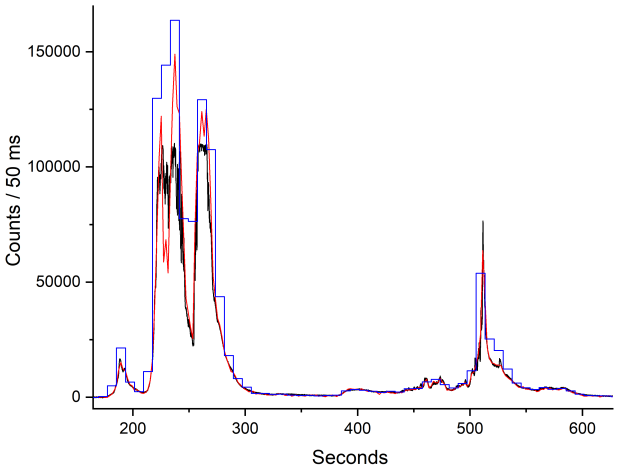

Fig. 3. Light curve of the main episode of GRB 221009A prompt emission as observed from INTEGRAL/ACS (in count rate unit). In black, we represent the original data (saturated), the red line shows the model calibrated against the *BepiColombo* detector, and in blue we plot the restored light curves using the INTEGRAL/IBIS-VETO detector. Our earliest optical observations closely resemble the epoch of the precursor activity and are the earliest optical observations ever reported for this historic burst.

3.2. Energetics

As we have discussed above, the burst was detected ~60° off the axis of the INTEGRAL spacecraft, so it became necessary to apply an off-axis correction before calculating the total energy of the burst. For the bursts that are not aligned with the telescope axis, the off-axis calibration was obtained from the bursts that are simultaneously detected by the *Fermi* and INTEGRAL spacecraft (Chelovekov et al. 2019; Pozanenko et al. 2020; Minaev & Pozanenko 2023). Utilizing a calibration method by Chelovekov et al. (2019), Pozanenko et al. (2020), Minaev & Pozanenko (2023), we converted the observed count rate into fluence, accounting for the off-axis angle (the angle between the direction toward the source and the X-axis of the INTEGRAL spacecraft, corresponding to the center of the field of view of the apertured instruments IBIS-ISGRI, SPI, JEM-X) and the peak energy (E_p) by assuming a cut-off power-law (CPL) model spectrum. It is important to note that these fluence values should be regarded as lower limits. Using the calibration method and the spectral model discussed above, we estimated the fluence in the 80–10 000 keV energy band for two characteristic energy types. For the soft energy spectrum (E_p = 500 keV), we obtained the fluence $F1 = 3.9^{+1.6}_{-1.2} \times 10^{-2}$ erg cm^{-2}, and for relatively harder spectrum (E_p = 1000 keV), we got the fluence $F2 = 2.0^{+0.6}_{-0.4} \times 10^{-2}$ erg cm^{-2}. Both of these estimates are lower than the fluence estimates published in other papers that were obtained with other experiments (e.g., the fluence in 1–10 000 keV energy range, obtained in Fermi/GMB by Lesage et al. 2023, is 9.5×10^{-2} erg cm^{-2}). Possible explanations are as follows: (1) The light curve in the IBIS/VETO detector used for dead time corrections is also affected by dead time effects. (2) The spectral response of the IBIS/VETO and ACS detectors is significantly different; that is, the spectral range of IBIS/VETO is shifted to a lower energy in comparison to the ACS nominal energy range 80 keV–10 MeV. This fluence represents an approximate seven-fold increase over GRB 130427A (at z = 0.34), previously the brightest event known before GRB 221009A, as reported by, for example, Ackermann et al. (2014), Maselli et al. (2014).

Table 2. Characteristics of a set of extensively examined TeV-detected GRBs sourced from various published papers, along with respective references provided in the final column.

GRB	z	T_{90} (s)	$E_{\gamma,iso}$ (erg)	SFR	log(M/M$_\odot$)	A_V (mag)	SN connection	References
GRB 160821B	0.162	1	2.10×10^{50}	1.20	8.5		KN	Lamb et al. (2019), Troja et al. (2019)
GRB 180720B	0.654	49	6.00×10^{53}	–	–		NO	Fraija et al. (2019b)
GRB 190114C	0.425	116	2.50×10^{53}	9.27	9.4	0.93	Yes	de Ugarte Postigo et al. (2020), Fraija et al. (2019a)
GRB 190829A	0.078	63	3.00×10^{50}	12.04	6.87	2.37	Yes	Hu et al. (2021), Gupta et al. (2022b)
GRB 201015A	0.426	9.78	3.86×10^{51}	–	–		Yes	Ror et al. (2023), Belkin et al. (2024)
GRB 201216C	1.1	29.9	6.32×10^{53}	–	–		NO	Ror et al. (2023)
GRB 221009A	0.151	327	$\sim1.00\times10^{55}$	9.70	1.20	0.12	Yes	This work, Lesage et al. (2023)

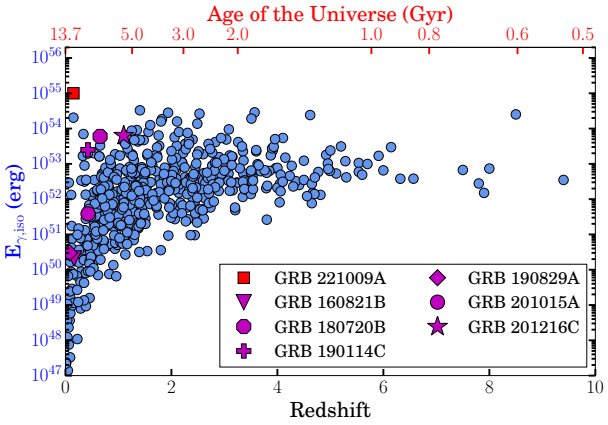

Fig. 4. Comparison of the relationship between the isotropic gamma-ray energy (Eγ, iso) distribution and the redshift (z) of GRB 221009A (red square) with other TeV-detected GRBs listed in Table 2. The background consists (blue circles) of a distribution of $E_{\gamma,iso}$ for a sample of GRBs with a measured z, taken from Minaev & Pozanenko (2020). The upper X-axis represents the age of the universe in giga years, corresponding to the redshift values indicated on the lower X-axis.

In our analysis, assuming unsaturated conditions, we calculated the isotropic gamma-ray energy ($E_{\gamma,iso}$) to be 1.5×10^{54} erg and 1.2×10^{54} erg for E_p values of 500 keV and 1 MeV, respectively. Both E_p scenarios are consistent with the Amati correlation for lGRBs, as detailed by Minaev & Pozanenko (2020). Relative to GRB 130427A, our findings indicate an approximate 1.5-fold increase in $E_{\gamma,iso}$. Additionally, we explored the relationship between the isotropic gamma-ray energy distribution and redshift (z) among TeV-detected GRBs (Table 2). Our analysis reveals that TeV-detected GRBs exhibit a broad range of energetics and adhere to the established relation, with GRB 221009A positioning it at the boundary of this relation (see Figure 4).

3.3. Redshift determination

In the GTC/OSIRIS stacked spectrum, the afterglow continuum is prominently detected across a wavelength range from 4000 Å to 9000 Å, showcasing an average S/N of ~85. Notably, as illustrated in Figure 1, at the bluer end of the spectrum, significant absorption can be observed, primarily attributable to the considerable Galactic extinction in the burst's direction, quantified as $E[B-V] = 1.30 \pm 0.06$ mag (Schlafly & Finkbeiner 2011). The spectrum is characterized by several absorption features, attributable to various systems from the Milky Way ($z = 0.0$) to the interstellar medium (ISM) of a galaxy at redshift $z = 0.1504 \pm 0.0001$. We identified this latter galaxy as the potential host of GRB 221009A based on the detection of the Ca II and Na I doublets. The redshift of the system is estimated from the centroid measurements of the host lines. We used a Gaussian fitting method to accurately identify the positions of the spectral lines and the error of each individual centroid, and then we computed the average, assuming that all of them come from the same cloud (refer to Table 3 and the left panel of Figure 1, de Ugarte Postigo et al. 2022; Castro-Tirado et al. 2022; Malesani et al. 2023).

As the afterglow faded, we observed the emergence of supernova signatures alongside emission lines from the underlying galaxy (Belkin et al. 2022b). Both in the 2D and 1D spectra, we identified an emission feature at the location anticipated for the Hα line of a galaxy at $z = 0.151$. This observation decisively links the observed emission and absorption lines – representing regions of hot and cold gas, respectively – to the same galaxy, as depicted in the right panel of Figure 1. These findings strongly constrain the GRB's redshift to $z \geq 0.151$, suggesting an association with the galaxy. Additionally, the absence of the Mg II doublet in our spectra sets an upper redshift limit of $z < 0.430$, reinforcing the connection between the GRB and the galaxy.

Table 3. Absorption line measurements from the OSIRIS afterglow spectrum.

Feature	λ_{obs} [Å] [(a)]	z	EW$_{rest}$ [Å] [(b)]	EW$_{lGRB}$ [Å] [(c)]
CaIIλ3935	4527.26 ± 0.37	0.1505756	1.78 ± 0.14	1.29 ± 0.31
CaIIλ3970	4566.69 ± 0.13	0.1504186	0.87 ± 0.10	0.93 ± 0.34
NaID [(d)]	6780.75 ± 0.27	0.1503387	0.38 ± 0.04	–

Notes. [(a)]λ_{obs} is the centroid of the line computed from a Gaussian fit. [(b)]EW$_{rest}$ represents the equivalent widths calculated at the rest frame. [(c)]EW$_{lGRB}$ is the average equivalent width typically observed in afterglow spectra of lGRBs (de Ugarte Postigo et al. 2012). [(d)]NaID denotes the blending of NaIλ5892 and NaIλ5898, which is not resolved in our spectra.

3.4. Absorption and emission line analysis

We calculated the equivalent widths (EWs) of the absorption lines from the ISM of the host galaxy of GRB 221009A (see Table 3). The Ca II H&K values from our spectrum are consistent with the values commonly found in lGRB hosts de Ugarte Postigo et al. (2012). Using the tight correlation EW(Na I) – E(B-V) existing in the Galaxy Poznanski et al. (2012), from the Na I doublet EW measurements, we inferred a host galaxy extinction of $E[B-V] = 0.039 \pm 0.007$. This scenario assumes that the host galaxy has an extinction law roughly similar to that of the Milky Way and fundamentally that the

Table 4. Emission line measurements from the BTA spectrum.

Feature	λ_{obs} [Å]	Flux [erg s^{-1} cm^{-2}]	Luminosity [erg s^{-1}]	EW$_{rest}$ [Å]
Hα	7560.20 ± 0.03	$(2.31 \pm 0.04) \times 10^{-15}$	$(1.51 \pm 0.03) \times 10^{41}$	–3.70 ± 0.10

Notes. The term λ_{obs} is the centroid of the line computed from a Gaussian fit. The flux and luminosity values have been corrected for Galactic extinction.

extinction in the line of sight is dominated by a diffuse interstellar component rather than by circumstellar dust.

Two absorption lines from the same species reside within the linear regime of the curve of growth (CoG) if the following relationship holds:

$$\frac{EW_1}{EW_2} = \frac{f_1 \lambda_{0,1}^2}{f_2 \lambda_{0,2}^2}, \quad (1)$$

where f_1 and f_2 are their oscillator strengths and $\lambda_{0,1}$ and $\lambda_{0,2}$ are their rest wavelengths. This Eq. (1) is valid for the Ca II lines, allowing us to reliably estimate the column density as log N(Ca II/cm^{-2}) = 13.30 ± 0.03. It is important to note that our column density measurement is less than the lower limit reported by Malesani et al. (2023). This is due to the discrepancy with the CaIIλ3970 measurement (~3.5σ), which places the Ca II ion in the saturated regime for their case. The substantial equivalent widths, alongside the absence of saturation, imply a significant effective Doppler parameter. This suggests the presence of a large galaxy with extensive kinematic breadth.

From the flux of the Hα emission line (Table 4), we obtained a luminosity of $L_{H\alpha} = 1.54 \pm 0.09$ erg s^{-1}, inferring an SFR of ~0.8 $M_\odot$ yr^{-1} Kennicutt & Evans (2012). From this measured SFR, we derived, using the correlations found by Belfiore et al. (2018) in the MaNGA sample of star-forming galaxies, a $\log(M_*/M_\odot) = 9.7 \pm 0.6$ (propagating SFR errors and dispersion of the relationship). Since this $L_{H\alpha}$ method is sensitive to the flux calibration accuracy, slit losses, and absorption in the line of sight, we also analyzed the EW of the $H\alpha$ line. Following Belfiore et al. (2018), we estimated an sSFR (which is a measure of the rate at which new stars are formed relative to the total stellar mass of the galaxy) for the host galaxy of log(sSFR) = –10.1 ± 0.2 yr^{-1}. Assuming the log(sSFR)−log(M_*) correlation suggested by Belfiore et al. (2018), we estimated a stellar mass of $\log(M_*/M_\odot) \sim 10.3$ (with a high intrinsic scatter), so SFR ~ 1.2 $M_\odot$ yr^{-1}. The magnitude limits of the host galaxy measured on images of the Pan-STARRS (PS1) survey are (g, r, i, z) > (22.0, 21.5, 21.4, 20.2). Using this information and the work by García-Benito et al. (2019), we can also impose an upper limit on the stellar mass, namely, $\log(M_*/M_\odot) < 10.0$, and it implies an SFR < 1.0 $M_\odot$ yr^{-1}. These results are consistent and also support the low host galaxy extinction inferred from the neutral sodium absorption. They are also compatible with Levan et al. (2023), Malesani et al. (2023).

3.5. Afterglow analysis

3.5.1. Early afterglow

The very early acquisition of optical observations significantly enhanced our comprehension of the mechanisms underlying GRBs. These observations are indispensable to probing the constitution of the fireball ejecta, helping pinpoint the emission locations of GRBs, discerning the central engine's activity, and elucidating the magnetization nature and the bulk Lorentz factor, among other fundamental aspects of GRB physics (Nakar & Piran 2004; Zhang & Kobayashi 2005; McMahon et al. 2006). Typically, early optical emission, which is external in origin, may explain phenomena such as reverse shock initiation, the onset of the afterglow, or even the manifestation of optical flash signatures within afterglow light curves (Mészáros & Rees 1999; Japelj et al. 2014; Gupta et al. 2021a). Nonetheless, cases of prompt optical emissions stemming from internal processes have been observed (Vestrand et al. 2005; Oganesyan et al. 2019).

Concerning GRB 221009A, optical observations were registered preceding the gamma-ray prompt emission (see Sections 2.2, and 2.3). Such data are exceedingly scarce, yet they are crucial for unraveling various enigmas surrounding GRBs (see Section 4.1 for more detail). Leveraging this dataset and augmenting it with external literature, we delved into the afterglow emission's evolution during the initial days in order to delineate some of the afterglow's physical characteristics (refer to Section 3.5.2 for further details). The convention for the evolution of afterglow flux with time and frequency is represented as $F(t, \nu) \propto t^\alpha \nu^\beta$.

3.5.2. Optical/X-ray afterglow light curve and spectral energy distribution

This section offers a comprehensive analysis of the multiwavelength afterglow of GRB 221009A, incorporating our early optical observations listed in Table A.1 alongside publicly available optical data sourced from GCN circulars[3] and various publications. The data include observations in the r, i, and z filters (Shrestha et al. 2023), Liverpool Telescope observations in the g, r, and i filters (Laskar et al. 2023); additional g, V, r, i, and z filter data (Kann et al. 2023); observations using the *HST* filters F625W and F775W (Levan et al. 2023); r, i, and z filter data (O'Connor et al. 2023); and R, J, H, and K data from Ror et al. (2024). The resultant multiband light curves are presented in Figure 5, which illustrates the comprehensive temporal coverage achieved by merging our initial R-band observations with subsequent publicly available observations, facilitating a robust fit using a smoothly joined broken power-law model. The early optical afterglow excludes any obvious flares and wiggles found, for example, in the bright afterglow of GRB 030329 (e.g., Mazaeva et al. 2018). The fit (optical R-band) yields power-law indices of $\alpha_{o1} = -0.56^{+0.04}_{-0.04}$, $\alpha_{o2} = -1.41^{+0.02}_{-0.02}$, with a break time of $t_{bo} = 24\,000^{+2600}_{-2550}$ s. The posterior distribution of the fit, depicted in Figure A.1 (upper panel), aligns well with findings from referenced studies (Shrestha et al. 2023; Laskar et al. 2023; Kann et al. 2023). The initial flat phase (pre-break) in the light curve suggests a prolonged activity of the central engine, transitioning into a steeper decline post break, which is indicative of the forward shock interacting with the external medium. In another scenario, an early jet break is also predicted at tb, as proposed by Levan et al. (2023), O'Connor et al. (2023). Our

[3] https://gcn.gsfc.nasa.gov/other/221009A.gcn3

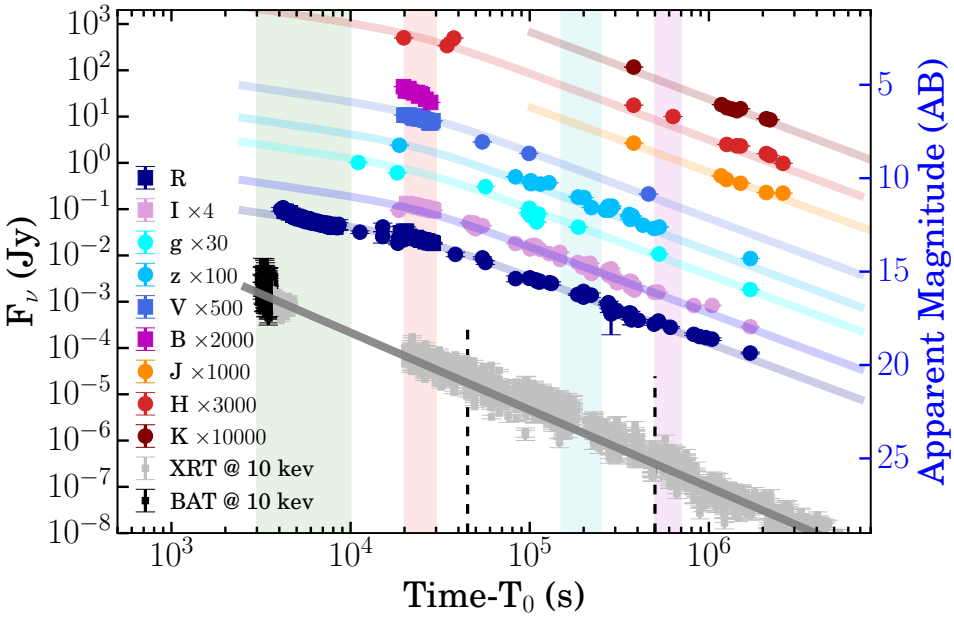

Fig. 5. Multiwavelength afterglow light curves of GRB 221009A. Optical data in various pass-bands has been scaled for clarity, as indicated by the legends in the lower-left corner. The data points in color-coded circles are those taken from the GCN circulars and other published articles, whereas those in Table A.1 are represented by color-coded squares. The solid lines overplotted on the observed data show the power laws fitted to the light curves, and the vertical black lines represent the segments in the XRT light curve that are separately fitted by a simple power law. The four colored regions denote the epochs of spectral energy distributions. The apparent magnitude is represented on the right-side Y-axis.

analysis did not identify a reverse shock component in the optical spectrum of GRB 221009A, although a reverse shock origin for radio emissions is proposed in Laskar et al. (2023). Due to the sparse data in the g, i, and z filters, we applied a simple power-law model, finding temporal decay indices consistent across these filters and matching the R-band light curve as well as a hint of a temporal break around $t_b \sim 24\,000$ s. Model fits to the g, i, z, J, H, and K band light curves are presented in Figure 5 as colored solid lines for visual guidance.

The X-ray light curve at 10 keV, sourced from the *Swift*-XRT database[4] (Evans et al. 2007, 2009), displays a power-law decay without notable features, such as flares. Fitting a simple power law to the data results in a decay index of $\alpha_x = -1.66^{+0.01}_{-0.01}$. Segmenting the light curve for further analysis revealed decay indices consistent within their error margins ($\alpha_{x1} = -1.63^{+0.03}_{-0.03}$, $\alpha_{x2} = -1.71^{+0.03}_{-0.03}$, and $\alpha_{x3} = -1.71^{+0.13}_{-0.13}$). Our fitting procedure confirms that a simple power law adequately models the *Swift*-XRT data, supporting conclusions drawn from similar analyses (Shrestha et al. 2023; Laskar et al. 2023; Kann et al. 2023). However, when applying a smoothly joined broken power law to the *Swift*-XRT curve, the resulting indices before and after the identified break time at $t_{bx} = 85\,000^{+12\,182}_{-15\,214}$ s, $\alpha_{x1} = 1.44^{+0.01}_{-0.01}$, and $\alpha_{x2} = 1.86^{+0.02}_{-0.02}$, display a discrepancy with segment-based analyses, highlighting challenges in constraining the break time, as shown in Figure A.1 (bottom panel).

Following the methodology outlined in Gupta et al. (2022a), Ror et al. (2023), we constructed joint optical to X-ray spectral energy distributions (SEDs) for four epochs across a series of observations. For the spectral fitting, we utilized XSPEC (Arnaud 1996) software. Each spectrum was then fitted by an absorption power-law model incorporating the absorption components *phabs* and *zphabs*, respectively proportional to the Galactic (NH_{Gal}) and host (NH_z) hydrogen column density along the line of sight of the observer. We took the value of the Galactic hydrogen column density $NH_{Gal} = 0.538 \times 10^{22}$ cm^{-25} from the *Swift* burst analyzer page (Evans et al. 2007, 2009), and it was further calculated from the NH_{Gal} map of Willingale et al. (2013). To constrain the value of the host absorption component NH_z, we retrieved the late time spectra in the temporal range 67 669 s to 101 193 s from the *Swift*-XRT webpage[6] (Evans et al. 2007, 2009). This is crucial because several features (e.g., flare, plateau, bumps, and pile-ups) present in the early afterglow light curve can reverberate the value of NH_z (Dalton & Morris 2020). By fitting the late time spectrum while keeping NH_z as a free parameter, we constrained the value of $NH_z = 1.430 \times 10^{22}$ cm^{-2}, which is very close to the value obtained by Williams et al. (2023) for the time-averaged spectrum in PC mode. For our subsequent analysis, the host and Galactic column densities were kept fixed at $NH_z = 1.430 \times 10^{22}$ cm^{-2} and $NH_{Gal} = 0.538 \times 10^{22}$ cm^{-2}, respectively.

The X-ray spectra for four distinct epochs (SED 1 at 3000–10 000 s, SED 2 at 20 000–30 000 s, SED 3 at 160 000–250 000 s, and SED 4 at 500 000–700 000 s) were retrieved from the *Swift*'s burst analyzer page (Evans et al. 2007, 2009). As discussed above, we utilized XSPEC software for the spectral fitting, using the absorption power-law model, but this time the host and Galactic column densities were kept fixed at $NH_z = 1.430 \times 10^{22}$ cm^{-2} and $NH_{Gal} = 0.538 \times 10^{22}$ cm^{-2}, respectively. Further, the test statistic C-stat was used to check for goodness of fit (Cash 1979). This analysis yielded spectral indices $\beta_{x1} = -0.67^{+0.02}_{-0.02}$, $\beta_{x2} = -0.80^{+0.02}_{-0.02}$, $\beta_{x3} = -0.74^{+0.06}_{-0.06}$, and $\beta_{x4} = -0.92^{+0.11}_{-0.11}$ for each epoch. The C-statistic (Cstat) and the corresponding degree of freedom (dof) for the four epochs respectively are 1203.7 and 962; 1022.5 and 924; 535.6 and 609; and 323.2 and 444. Our spectral fitting results are consistent with the results given in Table 1 of Williams et al. (2023) at similar epochs. For epochs SED 2, SED 3, and SED 4, ample multiband optical observations enabled us to derive optical spectral indices, obtaining $\beta_{o2} = -0.73^{+0.14}_{-0.14}$, $\beta_{o3} = -0.58^{+0.11}_{-0.11}$, and $\beta_{o4} = -0.23^{+0.11}_{-0.11}$.

Throughout the observation period, the X-ray spectral index β_x remained consistent with the closure relation for $\nu_x > \nu_c$, where $\beta_x = \frac{p}{2}$, with the electron energy distribution index p

[4] https://www.swift.ac.uk/burst_analyser/01126853/

[5] Given the very small redshift for GRB 221009A, the Galactic hydrogen column density and the intrinsic hydrogen column density are covariant in nature. We have noted that a larger NH_{Gal}, as suggested by Tiengo et al. (2023), would indeed result in a decrease in NH_z.

[6] https://www.swift.ac.uk/xrt_spectra/01126853/

constrained to approximately 1.6. This condition supports the notion of an early jet break and a particle distribution index less than two, as discussed in Gao et al. (2013). With this value of p, we can explain the temporal decay index $\alpha_x = \frac{3p+22}{16} \sim 1.6$ as a distribution in an ISM-like medium. However, the optical decay indices for the second and third epochs, α_o, correspond to the relation $\alpha_o = \frac{p+10}{8}$ in a wind-like medium for $\nu_o > \nu_c$.

In contrast, the last epoch's optical spectral index, $\beta_{o4} \sim 0.23$ (with $\Delta\beta \sim 0.5$), aligns with the spectral regime of $\nu_o < \nu_c$ $\left(\beta_o = \frac{p-1}{2}\right)$, and the optical decay index satisfies $\alpha_o = \frac{3(p+6)}{16}$ in an ISM-like medium. For scenarios where p is greater than two, as suggested by Shrestha et al. (2023), Kann et al. (2023), Laskar et al. (2023), O'Connor et al. (2023), decay indices in either ISM or wind-like media remain unexplained. Our findings indicate that a singular type of surrounding medium cannot account for the observed variations in light curve decay. Evidence supporting an early jet break and a transition from a wind-like to an ISM-like surrounding medium is also presented in Levan et al. (2023), O'Connor et al. (2023). This transition is consistent with previous findings in TeV-detected GRBs, such as those for GRB 190114C, where a similar transition was proposed by Fraija et al. (2019a). Detailed modeling of this medium transition, however, exceeds the scope of this study.

Our analysis revealed that over the last epochs examined, the X-ray spectral indices remained largely unchanged within errors. Conversely, the optical spectral indices exhibited a softening trend, signifying a notable alteration of approximately 0.5 in the spectral index around the epoch selected for SED 4. This observation aligns with the expected behavior of $\nu_c \propto t^{1/2}$ in a wind-like environment, following a post jet-break scenario. Such a scenario, as deduced from our study, concurs with findings reported in recent literature Ren et al. (2023), Shrestha et al. (2023), Levan et al. (2023), O'Connor et al. (2023).

Furthermore, the TripleSpec spectrum we obtained at +3.4 days post burst – close to the epoch selected for SED 3 in optical frequencies – predominantly shows continuum emission from the γ-ray burst afterglow, devoid of any discernible supernova absorption features. This case is in contrast to later photometric and spectroscopic analyses conducted beyond 20 days, which suggested underlying supernova features (Fulton et al. 2023; Blanchard et al. 2024). Therefore, to model our spectrum, we employed a power-law approximation $F_\nu \approx \nu^\beta$, using identical extinction coefficients as previously assumed. The best fit for our TripleSpec data suggests a power law with $\beta = -0.579 \pm 0.022$ (see Figure 2), indicating a marginally steeper decline than that observed in *JWST*/NIRSPEC measurements around ten days later, which presented $\beta = -0.362 \pm 0.001$ within the same spectral domain (Levan et al. 2024). This steepening trend is consistent with our optical spectra, providing further evidence for a temporal softening in the spectral hardness of the afterglow. Significantly, the timing of our TripleSpec observations – approximately 290 000 s post burst, closely aligning with SED 3 – affords an independent corroboration of the estimated optical spectral index of -0.58 ± 0.11. Additionally, our TripleSpec spectra are relatively insensitive to reddening, thereby underscoring the precision of our modeling approach.

3.6. GeV-TeV emission of GRB 221009A

GRB 221009A is notable for its exceptional brightness and broad spectral range, spanning radio to TeV energies. It is only the sixth lGRB to exhibit such extensive spectral emission, alongside GRB 180720B, GRB 190114C, GRB 190829A, GRB 201015A, and GRB 201216C. These rare GRBs, observed in both GeV and TeV energies, exhibit complex spectral features that challenge simple models (Miceli & Nava 2022). For instance, while some GRBs such as GRB 190829A have been modeled with a single synchrotron mechanism (H. E. S. S. Collaboration 2021), others such as GRB 190114C and GRB 180720B require additional synchrotron self-Compton components (MAGIC Collaboration 2019; Fraija et al. 2019b). The origin of GeV-TeV emissions remains debated, particularly regarding their internal versus external sources (Sahu et al. 2023; Wang et al. 2023; Berti & Carosi 2022; Gupta et al. 2021b). In the case of GRB 221009A, the detection of TeV photons coincides with the prompt emission phase, adding complexity to our understanding of GRB physics. The Large High Altitude Air Shower Observatory (LHAASO) reported around 5000 photons up to 18 TeV during the first 2000 seconds of the GBM trigger (Huang et al. 2022), later presenting the resulting time-dependent light curves for energies between 200 GeV and 7 TeV (LHAASO Collaboration 2023). The Carpet-2 mission also identified photons up to 250 TeV (Fraija et al. 2022). This very high energy detection provides insights into extragalactic background light (EBL) models and challenges standard physics. In this section, we explore the attenuation effects on TeV photons from GRB 221009A. Furthermore, we provide a comparative analysis of GRB 221009A with the other TeV-detected GRBs in Section 4.2.

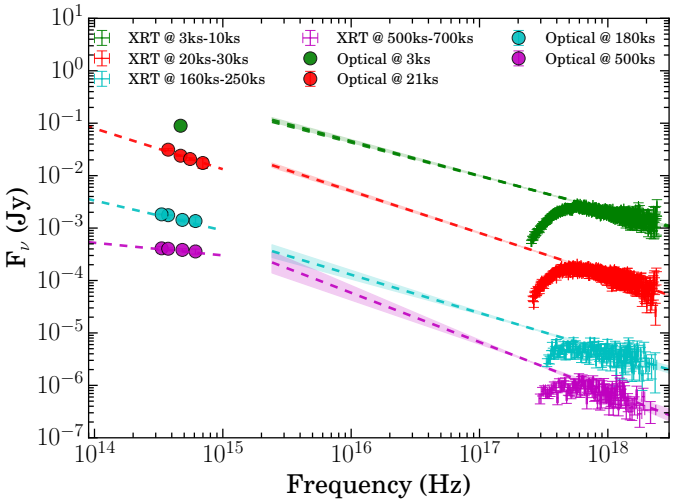

Fig. 6. Optical to X-ray SED corresponding to the time intervals shown by the color-coded vertical bands in the multiband afterglow light curves given in Figure 3. The dashed lines represent the power laws fitted to each spectrum, and values of indices obtained from the fitting are tabulated in Table 5. Optical observations shown here have been corrected for Galactic extinction.

3.6.1. Photon survival probability

To estimate the number of photons with energy around $E_{\rm min}$, we extrapolated the energy spectrum measured by LHAASO-WCDA for each observation period t^i, considering the lower limit on the spectral index and the upper limit on the flux normalization. The corresponding EBL absorption was applied, and the result was convoluted to the effective area and observation time of LHAASO-KM2A,

$$n_{\rm expect}\,(E_{\rm min}, z) = \sum_i \int_{E_{\rm min}}^{E_{\rm min}+1\sigma} dE J_0^i \left(\frac{E}{1\ {\rm GeV}}\right)^{-\Gamma^i} e^{-\tau(z,E)} A_{\rm eff}(E) \Delta t^i,$$

where $e^{-\tau(z,E)}$ is the attenuation for a given energy and distance, $\Delta t = (9, 8, 18, 574, 1100)$ s are the duration of the observation periods reported by LHAASO, and Γ^i and J_0^i are respectively the lower limit on the fitted spectral index and the upper limit on the fitted normalization of the spectrum of each observation period. The effective area, $A_{\rm eff}$, of LHAASO-KM2A was obtained from Aharonian & An (2021) and interpolated for the correct zenith angle of observation. The attenuation depends on the EBL model considered. In this calculation, we considered the Dominguez (2011) model in which upper and lower limits are provided, making it possible to evaluate the uncertainties coming from the EBL estimations Dominguez (2011). The probability of detecting at least one photon from a source at redshift z with energy around $E_{\rm min}$ can be calculated considering the expected Poissonian behavior of the measurement by

$$P^{1\gamma}_{E_{\rm min}}(z) = 1 - e^{n_{\rm expect}(E_{\rm min},z)}. \quad (2)$$

In the next subsection, we touch on other potential Lorentz invariance violation (LIV) effects on pair production for GRB 221009A.

3.6.2. Additional LIV considerations

We examined the LIV effects on pair production. We note that non-detection of photons above certain thresholds in the measured gamma-ray spectra can constrain LIV parameters (see Martínez-Huerta et al. 2020, and references therein). For example, under usual considerations, for $E^{(1)}_{\rm LIV} = 9.14 \times 10^{28}$ eV (current limits Lang et al. 2019), the expected number of photons around 1 PeV and 10 PeV was estimated to be on the order of 500. Thus, their non-detection would disfavor the LIV assumption, and limits on the LIV parameters can be established.

Moreover, a LIV hypothesis might imply varying speeds for photons of different energies (for example, higher energy photons have lower speeds in subluminal scenarios Addazi et al. 2022), leading to energy-dependent time delays (see Martínez-Huerta et al. 2020, and references therein). For instance, the expected time difference for photons of 1 MeV and 99.8 GeV is 13.53 (5.67×10^{-2}) s for $E_{\rm LIV} = 9.14 \times 10^{28}$ (2.18×10^{31}) eV and 7.51×10^{-2} (3.14×10^{-4}) s for 10 GeV and 18 TeV LHAASO photons. Still, more detailed investigations into the measured data and model are needed for exploring this and other LIV potential effects.

4. Discussion

4.1. Constraining GRB physics using the very early optical observations

We compiled a joint SED for the prompt emission, integrating data across optical and gamma-ray wavelengths from the early observations of GRB 221009A by the Mondy Observatory's all-sky camera (see Figure 7). The gamma-ray spectra from *Fermi* (spanning from T_0 +40 to T_0 +120 s) during the Mondy observations, characterized by a `Band function`, was derived by Ror et al. (2024). It is noteworthy that our optical observations are not directly related to the prompt gamma-ray spectrum captured by *Fermi*/GBM.

Our analysis suggests that GRB 221009A either lacks optical emissions of internal origin or possesses very faint optical emissions that fall below the Mondy Observatory all-sky camera's detection threshold. The non-detection of bright optical emissions of internal origin could be due to the overwhelming nature of the concurrent, bright prompt gamma-ray emission. Alternatively, the non-detection may result from the rapid variability of the internal origin, where the peak optical flux is extremely high but occurs within durations too brief to be detected within a 60-s exposure.

Table 5. Spectral indices obtained from fitting the SEDs given in the right panel of Figure 6.

Time (s)	β_o	β_x	p
SED 1 at 3000–10 000	–	$-0.67^{+0.02}_{-0.02}$	1.34 ± 0.04
SED 2 at 20 000–30 000	$-0.73^{+0.14}_{-0.14}$	$-0.80^{+0.02}_{-0.02}$	1.60 ± 0.04
SED 3 at 160 000–250 000	$-0.58^{+0.11}_{-0.11}$	$-0.74^{+0.06}_{-0.06}$	1.48 ± 0.12
SED 4 at 500 000–700 000	$-0.23^{+0.11}_{-0.11}$	$-0.92^{+0.11}_{-0.11}$	1.84 ± 0.22

In examining the possible reasons for the lack of early optical emissions with external origin, we assumed the same spectral regime and environmental density parameters as used in SED 1. By extrapolating the forward shock component's temporal decay, we estimated the expected optical brightness to be approximately 9.5 magnitudes at the time of the Mondy observations. Additionally, by considering the theoretically expected temporal decay (t^{-2} for ISM) from the thin shell external shock model's reverse-shock component, we estimated an expected brightness of approximately 4.5 magnitudes. The absence of early bright optical flash/reverse shock emissions linked to GRB 221009A suggests that the reverse shock component's emission either peaks at frequencies below the optical range or is obscured by the internal shock's prompt emissions.

We noted that for GRB 221009A, there is no early bump or peak observed in the optical light curve. Further analysis, using our earliest optical observation as an upper boundary for the peak time $t_{\rm peak}$, allowed us to establish a lower limit for the bulk Lorentz factor, $\Gamma_0 > 470$, using Eq. (4) of Ror et al. (2023). (For a detailed description of the methodology, see Molinari et al. 2007; Ror et al. 2023).

4.2. Comparison of GRB 221009A with other well-studied TeV lGRBs

After detecting TeV emission from GRB 221009A using LHAASO and Carpet-2, it became the sixth lGRB cataloged as having a TeV detection. Notably, GRB 160821B, an sGRB, is also in this list but with TeV photons below the 3-sigma threshold. GRB 221009A shows similarities to other TeV-detected bursts, as shown in Table 2, such as GRBs 190829A and 190114C, including two distinct prompt emissions: a modest precursor and a vivid multipulsed light curve. Among the TeV-detected GRBs, GRB 221009A has the longest prompt emission duration, potentially qualifying it as an ultra-lGRB (Ror et al. 2024). A comparative analysis revealed GRB 221009A's optical afterglow as the most luminous among TeV-detected GRBs and supernova-associated GRBs, with its X-ray afterglow also being exceptionally bright (see Figure A.2).

The TeV photons from GRB 180728B were detected about 10 hours post burst, while the nearest TeV burst, GRB 190829A, shows TeV photon detection starting 4 hours after the trigger and lasting three nights, making it the longest-duration TeV-detected burst (H. E. S. S. Collaboration 2021). GRB 190114C and GRB 201216C exhibit early TeV emission but with maximum energies around 1 TeV. In contrast, GRB 221009A's

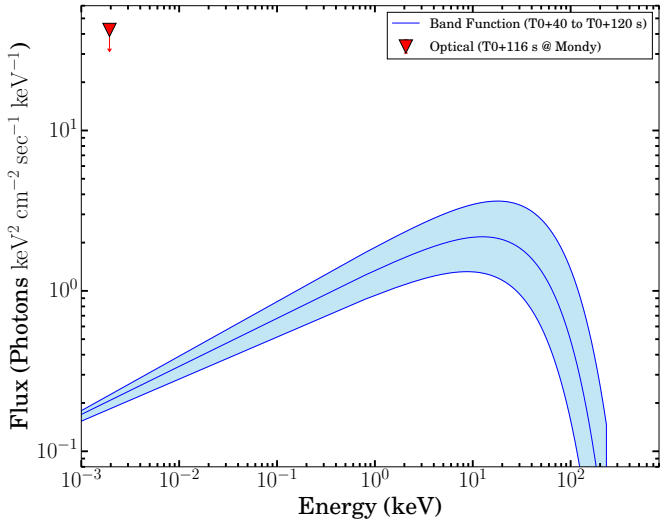

Fig. 7. Spectral energy distribution of prompt emission during the early optical observations of GRB 221009A taken with the all-sky camera at the Mondy telescope. The shaded blue region represents the uncertainty associated with the spectral parameters of the prompt emission. The *Fermi* spectrum (T_0 +40 to T_0 +120 s) during the Mondy observations, characterized by the best-fit `Band function`, is from Ror et al. (in prep.).

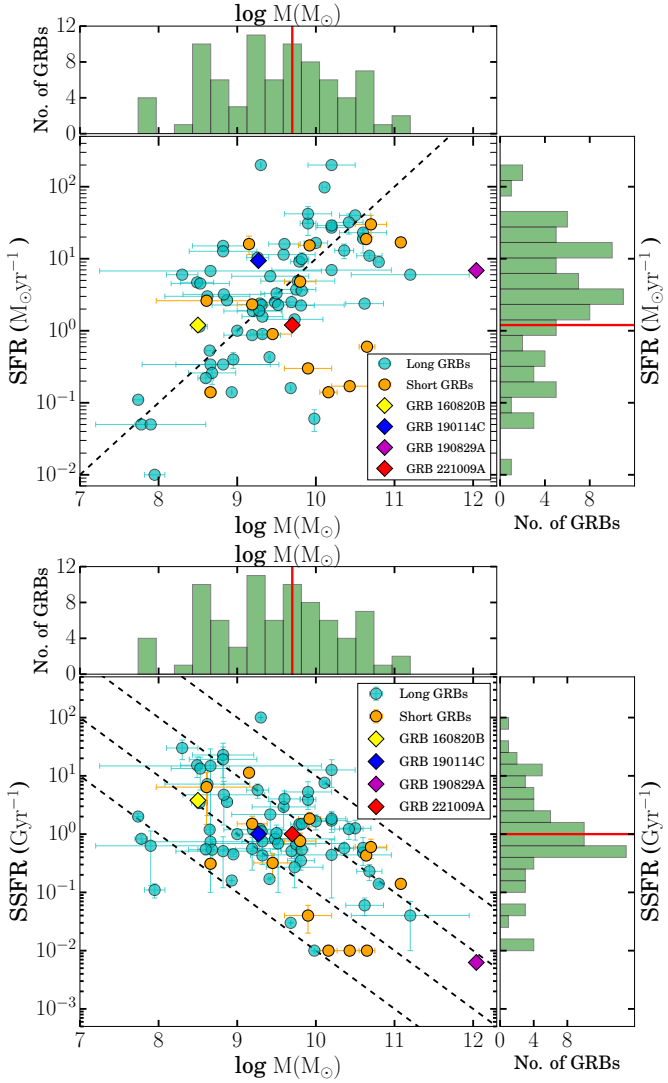

Fig. 8. Host galaxy characteristics of TeV GRBs presented along with other well-studied lGRBs (shown with cyan circles) and sGRBs (shown using orange circles) to determine if TeV-detected GRBs require unique environments. Top panel: Distribution of host galaxy mass plotted against SFR, with the top X-axis and right side Y-axis representing the histogram of mass and SFR, respectively. The dashed black line represents an sSFR of 1 Gyr^{-1} Bottom panel: Distribution of host galaxy mass as a function of sSFR, with the top X-axis and right side Y-axis representing the histogram of mass and sSFR, respectively. In these histograms, the vertical red lines show the position of GRB 221009A. The position of GRB 221009A is marked using red diamonds in both figures.

TeV photons, reaching around 250 TeV, challenge existing extragalactic background light models, leading some to suggest they may originate from Earth's atmosphere (Sahu et al. 2023). The origin of GRB 221009A's TeV photons is explained by reverse shock acceleration of electrons and protons in a high magnetic field (Zhang et al. 2023). Alternatively, a two-component jet model (Sato et al. 2023) and multiwavelength analysis (O'Connor et al. 2023) offer additional explanations. Recent studies also suggest that the environment around the burst might influence TeV emissions (Gupta et al. 2022b).

We conducted a thorough examination of the host galaxies associated with TeV-detected GRBs in order to ascertain whether these phenomena require distinct environments for the production of TeV photons. Figure 8 depicts a comparative analysis of host galaxy characteristics for TeV GRBs alongside extensively studied lGRBs and sGRBs. Our investigation encompassed an assessment of host galaxy mass in relation to SFR and sSFR for TeV-detected GRBs, with data points for lGRBs and sGRBs sourced from Savaglio et al. (2009). Remarkably, our findings indicate that the properties of host galaxies housing TeV-detected GRBs align with those observed for typical lGRBs and sGRBs. Furthermore, we identified striking similarities in the characteristics (mass, SFR, and sSFR) of the host galaxy of GRB 221009A with those of GRB 190114C.

4.3. Probing fundamental physics

Due to the EBL phenomenon, TeV photons experience cumulative attenuation, which increases with distance. Galactic sources in the TeV range are less affected, but extragalactic photons have a significantly reduced survival probability, leading to a strong suppression of gamma-ray flux on Earth. We estimated the detection probability of at least one photon, $P^{1\gamma}_{E_{\rm min}}$, from a source at the redshift of GRB 221009A. Results (including the confidence level equivalent for a double-sided Gaussian of the measurement not being explained by such assumptions on the right axis) are shown in the top panel of Figure 9, and they indicate a detection probability (affected by EBL modeling and LHAASO's energy resolution) of $P^{1\gamma}_{18\ \rm TeV}$ as 4.9×10^{-5} (4.06σ) under standard assumptions. The EBL uncertainties may shift this probability from 4.4×10^{-8} (5.47σ) to 6.2×10^{-3} (2.73σ). Energy resolution could further increase $P^{1\gamma}_{18\ \rm TeV}$ to 6.7×10^{-2}(1.83σ).

Thus, the 18 TeV GRB 221009A measurements may be explained by overestimation of energy and EBL distribution uncertainties, reaching $P^{1\gamma}_{12.85\ \rm TeV} = 0.991$ ($\approx 0.01\sigma$) in the most conservative scenario. New physics, such as LIV (Martínez-Huerta et al. 2020) or axion-like particles (ALPs) (Galanti & Roncadelli 2022), could also increase TeV photon survival by avoiding pair-production. The LIV scenarios, motivated by quantum gravity (QG) and string theories (see Addazi et al. 2022, and references therein), suggest that very

high energy photons can escape pair production, reducing attenuation above a certain energy (see Martínez-Huerta et al. 2020). The modulation of such effects is usually expressed by a LIV energy scale, $E^{(n)}_{\rm LIV}$, which can be associated with a QG or the Planck energy scale. Previous studies constrained $E^{(n)}_{\rm LIV}$ up to 10^{29} eV for $n = 1$ (Lang et al. 2019).

The bottom panel of Figure 9 shows the change in the probability of LHAASO detecting a photon around a given energy for different LIV assumptions. Considering the standard astrophysical assumptions, we found an increase in $P^{1\gamma}_{18\,\rm TeV}$ by a factor of 11.91× (5.47σ to 5.02σ) and of 3.34× (2.73σ to 2.41σ) for the most extreme scenarios of EBL and a LIV scenario compatible with current limits ($E^{n=1}_{\rm LIV} = 9.14 \times 10^{28}$ eV) (Lang et al. 2019).

We point out that although the survival probability in the LIV nominal scenario increases over the one with no LIV, as was exhibited here, this could be due to underestimating the energy and/or EBL uncertainties. This is compatible with other studies' outcomes and conclusions that have also reviewed the consequences of LIV scenarios due to detecting the 18 TeV photons from GRB 221009A (see, for instance, Finke & Razzaque 2023; Zheng et al. 2023; Baktash et al. 2022; Galanti et al. 2023; Kalashev et al. 2024).

5. Summary and conclusion

This paper presents a comprehensive analysis of the early photometric and spectroscopic observations of GRB 221009A, an exceptionally bright GRB detected by the INTEGRAL satellite, in conjunction with other high-energy missions, such as *Fermi* and *Swift*. For GRB 221009A, we have measured the highest photon fluence at the highest energies to date, saturating most of the high-energy instruments that detected this event. Our analysis of public INTEGRAL data yielded a fluence of approximately 100 erg cm^{-2}.

Utilizing our earliest GTC spectroscopic observations, we determined the redshift of GRB 221009A to be $z = 0.1504 \pm 0.0001$, consistent with previously published values. From this redshift, we derived an isotropic gamma-ray energy of approximately 10^{55} erg based on *Fermi* observations. Notably, GRB 221009A stands out among GRBs at this energy level, with the most similar events occurring at much greater distances.

Moreover, we investigated the link between isotropic gamma-ray energy and redshift for TeV-detected GRBs. While TeV-detected GRBs generally follow a typical relation, GRB 221009A deviates from this trend, lying at the edge of this relationship.

The aim of our analysis of very early photometric observations, obtained prior to the gamma-ray trigger by *Fermi*/GBM, was to constrain any early reverse shock emission or prompt optical emission. However, we found no evidence of early bright optical emission associated with GRB 221009A. We emphasize the importance of such early observations in investigating GRB physics, although they remain rare. The development of dedicated telescopes capable of synchronous multiwavelength observations during prompt emissions, such as the Space Variable astronomical Object Monitor (*SVOM*), is currently underway and will address this limitation.

Additionally, we examined the afterglow evolution through combined photometric and spectroscopic analyses. The early afterglow evolution suggests prolonged central engine activity and a density transition in the circumburst medium from a wind-like to an ISM-like environment, consistent with previous findings for GRB 190114C.

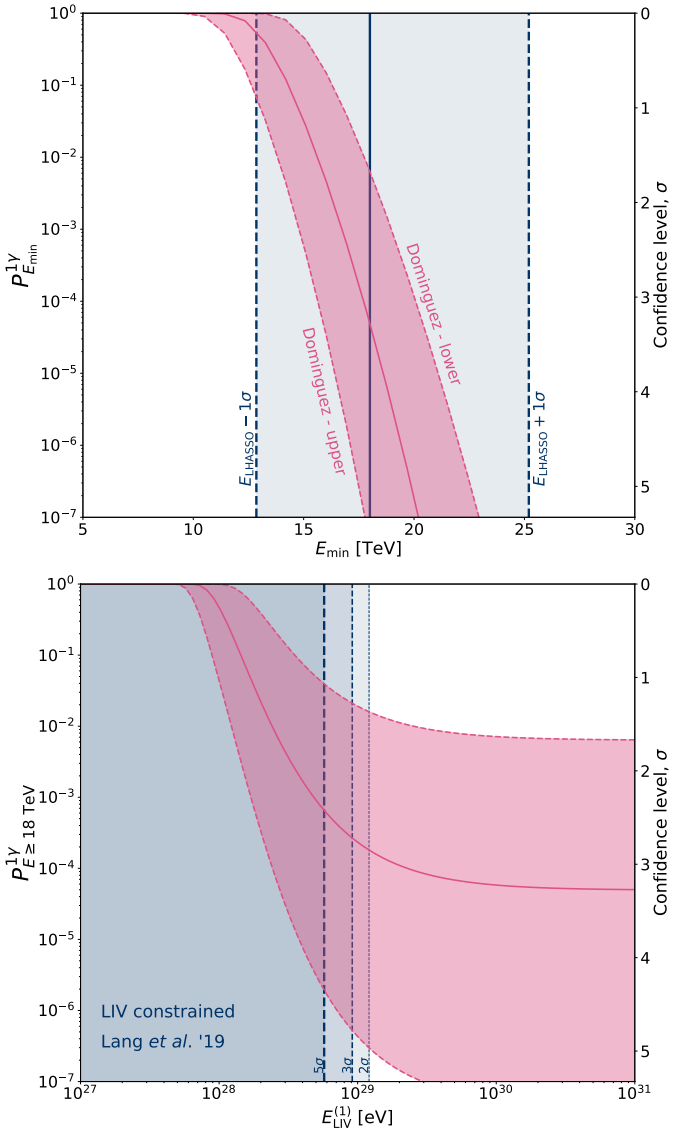

Fig. 9. Detection Probability of Single Photons and LIV Constraints in Gamma-Ray Astrophysics. Top: Probability of detecting at least a single photon with energy around $E_{\rm min}$, $P^{1\gamma}_{E_{\rm min}}$. The magenta band lines show the result for the Dominguez EBL model as well as its upper and lower limits. The solid blue line shows the energy measured by LHAASO at $E = 18$ TeV, and the blue band shows the energy region within 1 sigma of the energy resolution of the experiment (18 TeV ± 40%). Bottom: $P^{1\gamma}_{E_{\rm min}}$ with $E_{\rm min} = 18$ TeV as a function of the LIV energy scale. The magenta band again represents the EBL uncertainty. The blue shaded areas represent the phase space of $E_{\rm LIV}$ rejected with a 2, 3, and 5σ confidence level by the most competitive LIV limits coming from gamma-ray astrophysics.

We also studied the SED of the host galaxy of GRB 221009A, finding an SFR of $\sim$1 M$_\odot$ yr^{-1}, a stellar mass of $\log(M_*/M_\odot) \sim 9.5$, and low extinction along the line of sight. A comparative analysis of host galaxies associated with TeV-detected bursts and typical lGRBs and sGRBs revealed consistent characteristics, shedding light on the environments of TeV-detected GRBs.

Finally, the detection of TeV gamma-rays by LHAASO offered the opportunity to test new physics hypotheses, considering the expected propagation attenuation and the redshift determined for GRB 221009A. We evaluated the likelihood of

detecting such events under standard and new physics assumptions, such as LIV. In the nominal scenario, the survival probability, $P^{1\gamma}_{18\,\mathrm{TeV}}$, is 5.5 times higher than under standard assumptions. However, further investigation is needed to fully understand the nature of the extraordinary measurements from GRB 221009A and its potential as a test scenario for new physics.

Data availability

Full Table A.1 is available at the CDS via anonymous ftp to cdsarc.cds.unistra.fr (130.79.128.5) or via https://cdsarc.cds.unistra.fr/viz-bin/cat/J/A+A/692/A3

Acknowledgements. RSR acknowledges support under the CSIC-MURALES project with reference 20215AT009. RSR, YDH, MCG, SG, IPG, EJFG, RGB, MPV, and AJCT acknowledge financial support from the Spanish Ministry project PID2020-118491GB-I00 and from the Severo Ochoa grant CEX2021-001131-S funded by MCIN/AEI/ 10.13039/501100011033. Y-DH acknowledges support under the additional funding from the RYC2019-026465-I. MCG acknowledges support from the Ramón y Cajal Fellowship RYC2019-026465-I. BBZ acknowledges support by the National Key Research and Development Programs of China (2018YFA0404204, 2022SKA0130102, 2022YFF0711404), the National Natural Science Foundation of China (Grant Nos. 11833003, U2038105, 12121003), the science research grants from the China Manned Space Project with NO.CMS-CSST-2021-B11 and the Program for Innovative Talents, Entrepreneur in Jiangsu. MM acknowledges support from FAPERJ and CNPq. The work of FN, is supported by NOIRLab, which is managed by the Association of Universities for Research in Astronomy (AURA) under a cooperative agreement with the National Science Foundation. AP, SB, IC, SG, PM, NP, AV acknowledge support of Ministry of Science and Higher Education of the Russian Federation grant 075-15-2022-1221 (2022-BRICS-8847-2335). Observations with the SAO RAS telescopes are supported by the Ministry of Science and Higher Education of the Russian Federation. The renovation of telescope equipment is currently provided within the national project "Science and Universities". BTA observations were made under the ToO program (PI Pozanenko) under the quota of the Time Allocation Committee of Russian Telescopes. OAB thanks the Ministry of Higher Education, Science and innovation of the Republic of Uzbekistan for financial support, project no. IL-5421101855. CRB acknowledges the financial support from CNPq (316072/2021-4) and from FAPERJ (grants 201.456/2022 and 210.330/2022) and the FINEP contract 01.22.0505.00 (ref. 1891/22). Visiting Astronomer at the Infrared Telescope Facility, which is operated by the University of Hawaii under contract 80HQTR19D0030 with the National Aeronautics and Space Administration. Based in part on observations obtained at the Southern Astrophysical Research (SOAR) telescope, which is a joint project of the Ministério da Ciência, Tecnologia e Inovações (MCTI/LNA) do Brasil, the US National Science Foundation's NOIRLab, the University of North Carolina at Chapel Hill (UNC), and Michigan State University (MSU). SBP, RG, AKR, and AA acknowledge support from DST grant no. DST/ICD/BRICS/Call-5/CoNMuTraMO/2023(G) for the present work. RG was sponsored by the National Aeronautics and Space Administration (NASA) through a contract with ORAU. The views and conclusions contained in this document are those of the authors and should not be interpreted as representing the official policies, either expressed or implied, of the National Aeronautics and Space Administration (NASA) or the U.S. Government. The U.S. Government is authorized to reproduce and distribute reprints for Government purposes notwithstanding any copyright notation herein. This work was initiated with the support of the Finnish Geospatial Research Institute and the Academy of Finland project no. 325806 (PlanetS). The program of development within Priority-2030 is acknowledged for supporting the research at UrFU.

References

Ackermann, M., Ajello, M., Asano, K., et al. 2014, Science, 343, 42
Addazi, A., Alvarez-Muniz, J., Alves Batista, R., et al. 2022, Prog. Part. Nucl. Phys., 125, 103948
Afanasiev, V. L., & Moiseev, A. V. 2011, Balt. Astron., 20, 363
Aharonian, F., An, Q., Axikegu, et al. 2021, Chin. Phys. C, 45, 025002
Ahumada, T., Singer, L. P., Anand, S., et al. 2021, Nat. Astron., 5, 917
Akerlof, C., Balsano, R., Barthelmy, S., et al. 1999, Nature, 398, 400
Arnaud, K. A. 1996, ASP Conf. Ser., 101, 17
Baktash, A., Horns, D., & Meyer, M. 2022, arXiv e-prints [arXiv:2210.07172]
Belfiore, F., Maiolino, R., Bundy, K., et al. 2018, MNRAS, 477, 3014
Belkin, S., Pozanenko, A., Klunko, E., Pankov, N., & GRB IKI FuN 2022a, GCN, 32645, 1
Belkin, S., Moskvitin, A., Kim, V., et al. 2022b, GCN, 32818, 1
Belkin, S., Pozanenko, A. S., Minaev, P. Y., et al. 2024, MNRAS, 527, 11507
Berti, A., & Carosi, A. 2022, Galaxies, 10, 67
Blanchard, P. K., Villar, V. A., Chornock, R., et al. 2024, Nat. Astron., 8, 774
Burns, E., Svinkin, D., Fenimore, E., et al. 2023, ApJ, 946, L31
Caballero-García, M. D., Gupta, R., Pandey, S. B., et al. 2023, MNRAS, 519, 3201
Cash, W. 1979, ApJ, 228, 939
Castro-Tirado, A. J. 2023, Nat. Astron., 7, 1136
Castro-Tirado, A. J., Sanchez-Ramirez, R., Hu, Y. D., et al. 2022, GCN, 32686, 1
Cepa, J., Aguiar, M., Escalera, V. G., et al. 2000, SPIE Conf. Ser., 4008, 623
Chelovekov, I. V., Grebenev, S. A., Pozanenko, A. S., & Minaev, P. Y. 2019, Astron. Lett., 45, 635
Cushing, M. C., Vacca, W. D., & Rayner, J. T. 2004, PASP, 116, 362
Dalton, T., & Morris, S. L. 2020, MNRAS, 495, 2342
de Ugarte Postigo, A., Fynbo, J. P. U., Thöne, C. C., et al. 2012, A&A, 548, A11
de Ugarte Postigo, A., Thöne, C. C., Martín, S., et al. 2020, A&A, 633, A68
de Ugarte Postigo, A., Izzo, L., Pugliese, G., et al. 2022, GCN, 32648, 1
Dichiara, S., Gropp, J. D., Kennea, J. A., et al. 2022, ATel, 15650, 1
Dominguez, A., et al. 2011, MNRAS, 410, 2556
Evans, P. A., Beardmore, A. P., Page, K. L., et al. 2007, A&A, 469, 379
Evans, P. A., Beardmore, A. P., Page, K. L., et al. 2009, MNRAS, 397, 1177
Finke, J. D., & Razzaque, S. 2023, ApJ, 942, L21
Fraija, N., Dichiara, S., Pedreira, A. C. C. d. E. S., et al. 2019a, ApJ, 879, L26
Fraija, N., Dichiara, S., Pedreira, A. C. C. d. E. S., et al. 2019b, ApJ, 885, 29
Fraija, N., Gonzalez, M., & HAWC Collaboration 2022, ATel, 15675, 1
Frederiks, D., Svinkin, D., Lysenko, A. L., et al. 2023, ApJ, 949, L7
Fulton, M. D., Smartt, S. J., Rhodes, L., et al. 2023, ApJ, 946, L22
Galanti, G., & Roncadelli, M. 2022, Universe, 8, 253
Galanti, G., Roncadelli, M., & Tavecchio, F. 2023, Phys. Rev. Lett., 131, 251001
Gao, H., Lei, W.-H., Zou, Y.-C., Wu, X.-F., & Zhang, B. 2013, New Astron., 57, 141
García-Benito, R., González Delgado, R. M., Pérez, E., et al. 2019, A&A, 621, A120
Gehrels, N., Chincarini, G., Giommi, P., et al. 2004, ApJ, 611, 1005
Gotz, D., Mereghetti, S., Savchenko, V., et al. 2022, GCN, 32660, 1
Gupta, R., Oates, S. R., Pandey, S. B., et al. 2021a, MNRAS, 505, 4086
Gupta, R., Pandey, S. B., Castro-Tirado, A. J., et al. 2021b, Rev. Mex. Astron. Astrofis. Conf. Ser., 53, 113
Gupta, R., Gupta, S., Chattopadhyay, T., et al. 2022a, MNRAS, 511, 1694
Gupta, R., Pandey, S. B., Kumar, A., et al. 2022b, JApA, 43, 82
H. E. S. S. Collaboration (Abdalla, H., et al.) 2021, Science, 372, 1081
Hu, Y. D., Castro-Tirado, A. J., Kumar, A., et al. 2021, A&A, 646, A50
Hu, Y. D., Casanova, V., Fernandez-Garcia, E., et al. 2022, GCN, 32644, 1
Huang, Y., Hu, S., Chen, S., et al. 2022, GCN, 32677, 1
Japelj, J., Kopač, D., Kobayashi, S., et al. 2014, ApJ, 785, 84
Kalashev, O., Aharonian, F., Essey, W., Inoue, Y., & Kusenko, A. 2024, arXiv e-prints [arXiv:2405.05402]
Kann, D. A., Agayeva, S., Aivazyan, V., et al. 2023, ApJ, 948, L12
Kennea, J. A., Williams, M., & Swift, 2022, Team., GCN, 32635, 1
Kennicutt, R. C., & Evans, N. J. 2012, ARA&A, 50, 531
Kouveliotou, C., Meegan, C. A., Fishman, G. J., et al. 1993, ApJ, 413, L101
Kozyrev, A. S., Golovin, D. V., Litvak, M. L., et al. 2022, GCN, 32805, 1
Lamb, G. P., Tanvir, N. R., Levan, A. J., et al. 2019, ApJ, 883, 48
Lang, R. G., Martínez-Huerta, H., & de Souza, V. 2019, Phys. Rev. D, 99, 043015
Laskar, T., Alexander, K. D., Margutti, R., et al. 2023, ApJ, 946, L23
Lesage, S., Veres, P., Briggs, M. S., et al. 2023, ApJ, 952, L42
Levan, A. J., Lamb, G. P., Schneider, B., et al. 2023, ApJ, 946, L28
Levan, A., Gompertz, B. P., Salafia, O. S., et al. 2024, Nature, 626, 737
LHAASO Collaboration (Cao, Z., et al.) 2023, Science, 380, 1390
MAGIC Collaboration (Acciari, V. A., et al.) 2019, Nature, 575, 459
Malesani, D. B., Levan, A. J., Izzo, L., et al. 2023, A&A, submitted [arXiv:2302.07891]
Martínez-Huerta, H., Lang, R. G., & de Souza, V. 2020, Symmetry, 12, 1232
Maselli, A., Melandri, A., Nava, L., et al. 2014, Science, 343, 48
Mazaeva, E., Pozanenko, A., & Minaev, P. 2018, IJMPD, 27, 1844012
McMahon, E., Kumar, P., & Piran, T. 2006, MNRAS, 366, 575
Mészáros, P., & Rees, M. J. 1997, ApJ, 476, 232
Mészáros, P., & Rees, M. J. 1999, MNRAS, 306, L39
Miceli, D., & Nava, L. 2022, Galaxies, 10, 66
Minaev, P. Y., & Pozanenko, A. S. 2020, MNRAS, 492, 1919
Minaev, P. Y., & Pozanenko, A. S. 2023, MNRAS, 525, 2411
Molinari, E., Vergani, S. D., Malesani, D., et al. 2007, A&A, 469, L13
Nakar, E., & Piran, T. 2004, MNRAS, 353, 647
O'Connor, B., Troja, E., Ryan, G., et al. 2023, Sci. Adv., 9, eadi1405
Oganesyan, G., Nava, L., Ghirlanda, G., Melandri, A., & Celotti, A. 2019, A&A, 628, A59

Pandey, S. B., & Zheng, W. 2013, EAS Publ. Ser., 61, 203
Piran, T. 2004, Rev. Mod. Phys., 76, 1143
Pozanenko, A. S., Minaev, P. Y., Grebenev, S. A., & Chelovekov, I. V. 2020, Astron. Lett., 45, 710
Poznanski, D., Prochaska, J. X., & Bloom, J. S. 2012, MNRAS, 426, 1465
Rastinejad, J. C., Gompertz, B. P., Levan, A. J., et al. 2022, Nature, 612, 223
Ren, J., Wang, Y., & Zhang, L.-L. 2023, ApJ, 947, 53
Ror, A. K., Gupta, R., Jelínek, M., et al. 2023, ApJ, 942, 34
Ror, A. K., Gupta, R., Aryan, A., et al. 2024, ApJ, 971, 163
Sahu, S., Medina-Carrillo, B., Sánchez-Colón, G., & Rajpoot, S. 2023, ApJ, 942, L30
Sari, R., Piran, T., & Narayan, R. 1998, ApJ, 497, L17
Sato, Y., Obayashi, K., Theodre Zhang, B., et al. 2023, J. High Energy Astrophys., 37, 51
Savaglio, S., Glazebrook, K., & Le Borgne, D. 2009, ApJ, 691, 182
Schlafly, E. F., & Finkbeiner, D. P. 2011, ApJ, 737, 103
Schlawin, E., Herter, T. L., Henderson, C., et al. 2014, SPIE Conf. Ser., 9147, 91472H
Shrestha, M., Sand, D. J., Alexander, K. D., et al. 2023, ApJ, 946, L25
Tiengo, A., Pintore, F., Vaia, B., et al. 2023, ApJ, 946, L30
Tody, D. 1986, SPIE Conf. Ser., 627, 733
Tody, D. 1993, ASP Conf. Ser., 52, 173
Troja, E., Castro-Tirado, A. J., Becerra González, J., et al. 2019, MNRAS, 489, 2104
Troja, E., Fryer, C. L., O'Connor, B., et al. 2022, Nature, 612, 228
Vacca, W. D., Cushing, M. C., & Rayner, J. T. 2003, PASP, 115, 389
Veres, P., Burns, E., Bissaldi, E., et al. 2022, GCN, 32636, 1
Vestrand, W. T., Wozniak, P. R., Wren, J. A., et al. 2005, Nature, 435, 178
Wang, K., Ma, Z.-P., Liu, R.-Y., et al. 2023, Sci. China: Phys. Mech. Astron., 66, 289511
Williams, M. A., Kennea, J. A., Dichiara, S., et al. 2023, ApJ, 946, L24
Willingale, R., Starling, R. L. C., Beardmore, A. P., Tanvir, N. R., & O'Brien, P. T. 2013, MNRAS, 431, 394
Zhang, B., & Kobayashi, S. 2005, ApJ, 628, 315
Zhang, B. T., Murase, K., Ioka, K., et al. 2023, ApJ, 947, L14
Zheng, Y. G., Kang, S. J., Zhu, K. R., Yang, C. Y., & Bai, J. M. 2023, Phys. Rev. D, 107, 083001

[1] Instituto de Astrofísica de Andalucía, Consejo Superior de Investigaciones Científicas (IAA-CSIC), Glorieta de la Astronomía, s/n, 18080 Granada, Spain
[2] Erlangen Centre for Astroparticle Physics, Friedrich-Alexander-Universität Erlangen-Nürnberg, Nikolaus-Fiebiger-Str. 2, Erlangen D-91058, Germany
[3] Space Research Institute, Russian Academy of Sciences, Profsoyuznaya, 84/32, Moscow 117997, Russia
[4] Higher School of Economics, National Research University, Myasnitskaya 20, Moscow 101000, Russia
[5] Moscow Institute of Physics and Technology (MIPT), Institutskiy Pereulok, 9, Dolgoprudny 141701, Russia
[6] Departamento de Física y Matemáticas, Universidad de Monterrey, Avda. Morones Prieto 4500, San Pedro Garza García, 66238 Nuevo León, Mexico
[7] Aryabhatta Research Institute of Observational Sciences (ARIES), Manora Peak, Nainital 263002, Uttarakhand, India
[8] Astrophysics Science Division, NASA Goddard Space Flight Center, Mail Code 661, Greenbelt, MD 20771, USA
[9] NASA Postdoctoral Program Fellow, Greenbelt, MD 20771, USA
[10] School of Astronomy and Space Science, Nanjing University, Nanjing 210093, China
[11] Key Laboratory of Modern Astronomy and Astrophysics (Nanjing University), Ministry of Education, Nanjing 210093, China
[12] School of Physics and Astronomy & Institute for Gravitational Wave Astronomy, University of Birmingham, Birmingham, B15 2TT, UK
[13] Petro Mohyla Black Sea National University, 68 Desantnykiv Street, 10, Mykolaiv 54003, Ukraine
[14] Laboratório Nacional de Astrofísica, Itajubá, MG, Brazil
[15] Centro Brasileiro de Pesquisas Físicas, Rua Dr. Xavier Sigaud 150, Rio de Janeiro 22290-180, RJ, Brazil
[16] Centro Federal de Educação Tecnológica Celso Suckow da Fonseca, Rodovia Mário Covas, lote J2, quadra J, Itaguaí 23810-000, RJ, Brazil
[17] East Tennessee State University, 1276 Gilbreath Dr., Box 70300, Johnson City 37614, TN, USA
[18] Ulugh Beg Astronomical Institute, Uzbek Academy of Sciences, Tashkent, Uzbekistan
[19] Unidad Asociada al CSIC, Dpto. de Ingeniería de Sistemas y Automática, Escuela de Ingenierías, Universidad de Málaga, C/ Dr. Ortiz Ramos, s/n, Málaga 29071, Spain
[20] Center for Interdisciplinary Exploration and Research in Astrophysics (CIERA), Northwestern University, Evanston 60208, IL, USA
[21] Institute of Solar-Terrestrial Physics, Russian Academy of Sciences, Siberian Branch, Irkutsk, Russia
[22] International Center for Advanced Studies & Instituto de Ciencias Físicas, ECyT-UNSAM & CONICET, Buenos Aires 1650, Argentina
[23] Special Astrophysical Observatory, Russian Academy of Sciences, Nizhnii Arkhyz 369167, Russia
[24] SOAR Telescope, NSF's NOIRLab, Avda. Juan Cisternas, 1500, La Serena 1700000, Chile
[25] Austin Peay State University, 601 College St, Clarksville 37044, TN, USA
[26] Department of Astronomy and Astrophysics, University of California, Santa Cruz 95064, CA, USA
[27] Fermi National Accelerator Laboratory, P. O. Box 500, Batavia 60510, IL, USA
[28] Benedictine University, 5700 College Road, Lisle, IL, USA
[29] Swedish Institute of Space Physics (IRF), Bengt Hultqvists väg 1, 981 92 Kiruna, Sweden
[30] Faculty of Science, University of Helsinki, Gustaf Hallströmin katu 2, FI-00014 Helsinki, Finland
[31] Institute of Physics and Technology, Ural Federal University, Mira str. 19, 620002 Ekaterinburg, Russia
[32] Department of Applied Physics/Physics, Mahatma Jyotiba Phule Rohilkhand University, Bareilly-243006, India
[33] Petrozavodsk State University, Petrozavodsk, Russia
[34] School of Physics & Astronomy, Monash University, Clayton, VIC 3800, Australia
[35] INAF - Osservatorio Astronomico di Brera, Via E. Bianchi 46, 23807 Merate (LC), Italy

Appendix A: Additional material

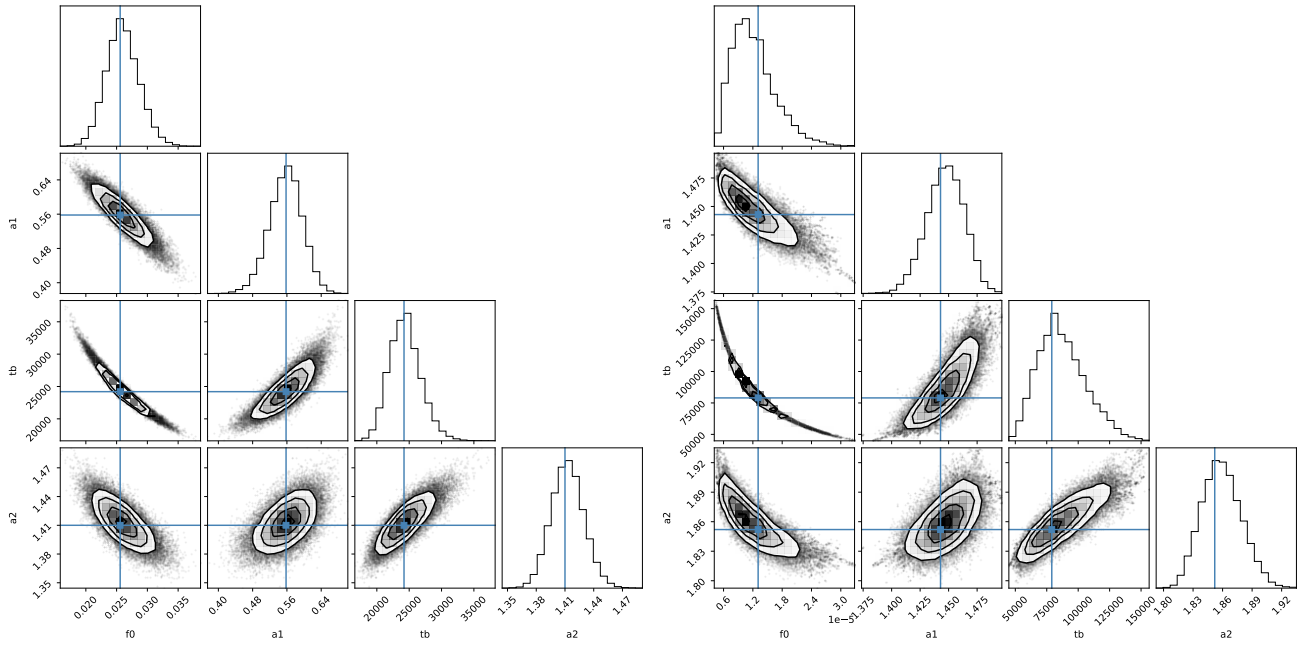

Fig. A.1. Posterior parameter distribution obtained by fitting a smoothly joined broken power law to the R-band (top) and *Swift*-XRT light curve (bottom).

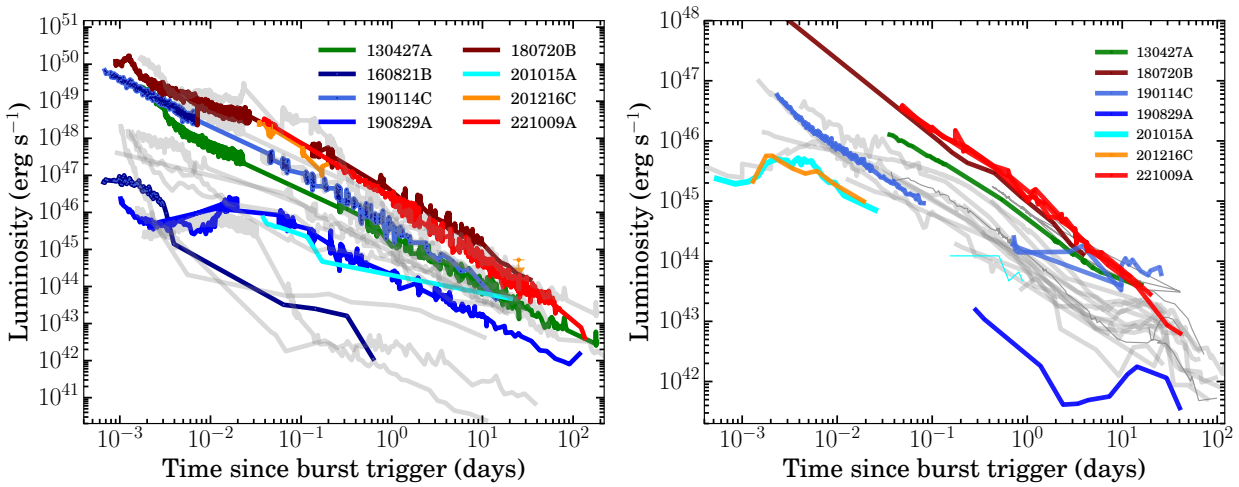

Fig. A.2. Comparison of XRT and R-band Luminosity Light Curves of TeV-detected and Supernova-associated GRBs. *Top*: *Swift*-XRT luminosity light curve of TeV-detected GRBs (plotted in various colors) and nearby GRBs that have observed supernova emission (gray color in the background). To compare the brightness of GRB 130427A and GRB 221009A, GRB 130427A is also added. *Bottom*: R-band luminosity light curves of TeV-detected GRBs are similarly plotted with the supernovae-detected GRBs in the background.

Table A.1. Optical observations of GRB 221009A (extract). The full table is available at the CDS.

Start time (UT)	T-T$_0$ (s)	Exp. (s)	Filter	mag^{a,b} (AB)	Telescope
2022-10-09T13:14:23	-126	60	Clear	>6	Mondy
2022-10-09T13:16:24	-5	60	Clear	>6	Mondy
2022-10-09T13:18:25	116	60	Clear	>6	Mondy
...	...	...	...	...	...

Notes.
[a]Magnitudes are not corrected for Galactic extinction.
[b]The magnitude errors are given at the 1σ level.